Journal of ELECTRONIC MATERIALS, Vol. 45, No. 9, 2016
DOI: 10.1007/s11664-016-4702-3
© 2016 The Author(s). This article is published with open access at Springerlink.com

Status of HgCdTe Barrier Infrared Detectors Grown by MOCVD in Military University of Technology

M. KOPYTKO,[1,2] K. JÓŹWIKOWSKI,[1] P. MARTYNIUK,[1] W. GAWRON,[1] P. MADEJCZYK,[1] A. KOWALEWSKI,[1] O. MARKOWSKA,[1] A. ROGALSKI,[1] and J. RUTKOWSKI[1]

1.—Institute of Applied Physics, Military University of Technology, 2 Kaliskiego Str., 00-908 Warsaw, Poland. 2.—e-mail: malgorzata.kopytko@wat.edu.pl

In this paper we present the status of HgCdTe barrier detectors with an emphasis on technological progress in metalorganic chemical vapor deposition (MOCVD) growth achieved recently at the Institute of Applied Physics, Military University of Technology. It is shown that MOCVD technology is an excellent tool for HgCdTe barrier architecture growth with a wide range of composition, donor/acceptor doping, and without post-grown annealing. The device concept of a specific barrier bandgap architecture integrated with Auger-suppression is as a good solution for high-operating temperature infrared detectors. Analyzed devices show a high performance comparable with the state-of-the-art of HgCdTe photodiodes. Dark current densities are close to the values given by "Rule 07" and detectivities of non-immersed detectors are close to the value marked for HgCdTe photodiodes. Experimental data of long-wavelength infrared detector structures were confirmed by numerical simulations obtained by a commercially available software APSYS platform. A detailed analysis applied to explain dark current plots was made, taking into account Shockley–Read–Hall, Auger, and tunneling currents.

Key words: Infrared detectors, barrier detectors, HgCdTe, MOCVD

INTRODUCTION

At present, one of the leading topics in high-operating temperature (HOT) infrared (IR) detectors are barrier devices, including *n*B*n* and *p*B*n* design.[1–4] Barrier detectors in such configuration require a proper bandgap engineering. The structure should have a large offset in one band and a zero offset in the other. Such a barrier arrangement blocks one carrier type (electron or hole) and allows the unimpeded flow of the other. Barriers should be located near the minority carrier collector and away from the region of optical absorption. Zero offset in one band allows photogenerated holes to flow to the contact (cathode) while the majority carrier dark current, re-injected photocurrent, and surface current are blocked by the barrier.[5] Thus, the barrier detector is designed to reduce dark current associated with Shockley–Read–Hall (SRH) generation-recombination (GR) processes and noise without impending photocurrent (signal).

Despite all the advantages of barrier detectors outlined above, the implementation of this detector structure in the HgCdTe ternary material system is not straightforward due to the existence of a valence band discontinuity (barrier) at the absorber–barrier interface. Non-zero valence band offset in HgCdTe *n*B*n* detector structures is the key item limiting their performance.[6–11] Devices exhibit poor responsivity and detectivity, especially at low temperatures,[6] where the low-energy minority carriers generated by optical absorption are not able to overcome the valence band energy barrier (ΔE_V) (see Fig. 1a). Depending on the wavelength of operation, a relatively high bias—typically greater than the bandgap energy—is required to be applied to the device to collect all of the photogenerated

(Received October 22, 2015; accepted May 26, 2016; published online June 30, 2016)

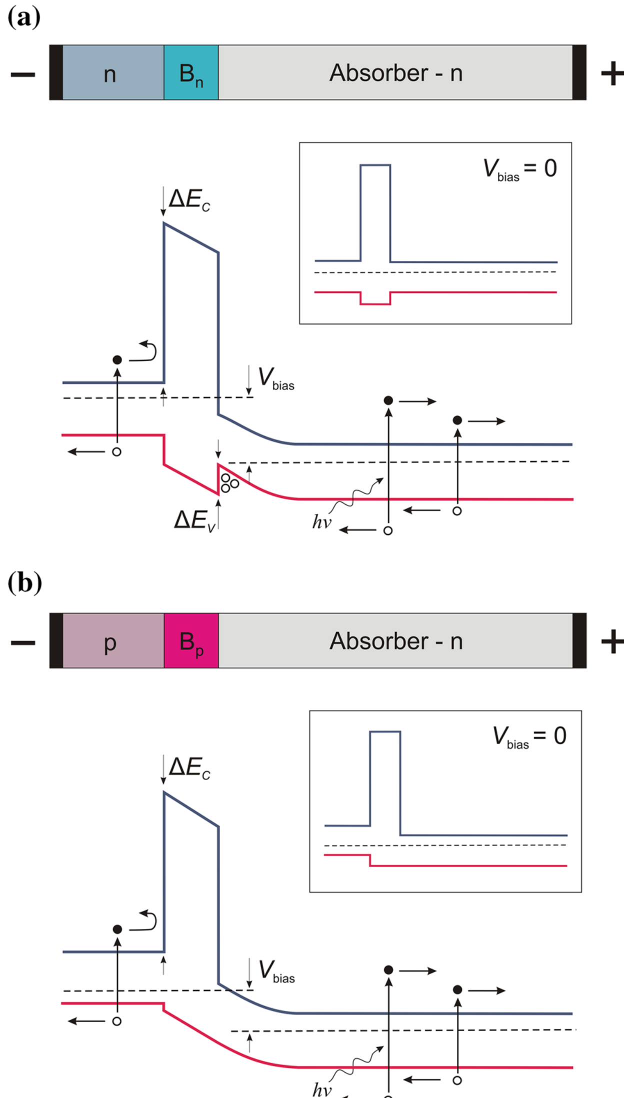

Fig. 1. Schematic band diagrams of HgCdTe barrier detectors with (a) nonzero and (b) zero valence band offset.

carriers. However, this might lead to strong band-to-band and trap-assisted tunneling (TAT) due to high electric field within the depletion layer.

Reduction of valence band offsets to a reasonably low value, by the adjustment of the Cd mole fraction in the barrier, results in a corresponding reduction of the barrier in the conduction band (ΔE_C) below a critical level, thus increasing the majority carrier dark current at high temperatures. This also leads to the photoelectric gain.[12] The responsivity increases when the reverse bias is applied.[13] In HgCdTe material, proper *p*-type doping of the barrier reduces the valence band-offset and increases the offset in the conduction band.[14–17]

The device with the barrier only in the conduction band is similar to that proposed in Ref. 1 in which a *p*-type barrier is interposed between two narrow gap *n*-type regions. Furthermore, due to the presence of the barrier, it is possible to replace *n*-type cap contact by the *p*-type layer (Fig. 1b) without affecting the dark current. It is similar to one of the realizations of III–V semiconductor-based devices and named *X*B*n* structures,[3,4] in which *X* stands for the *n*- or *p*-type contact layer.

To overcome HgCdTe band offset issues, the band gap discontinuity should be efficiency eliminated by grading of the barrier composition and doping density profiles.[14–17]

This paper presents the status of MOCVD-grown HgCdTe barrier detectors, with emphasis on technological achievements in removing the valence band offset made recently at the Institute of Applied Physics, Military University of Technology (MUT).[17–19]

DEVICE DESIGN AND FABRICATION

The epitaxial structures were grown in a joint laboratory run by VIGO System S.A. and MUT. In our laboratory, the growth of HgCdTe layers is carried out using the interdiffused multilayer process in a horizontal, near atmospheric pressure MOCVD AIX 200 reactor provided by Aixtron. One of the merits of MOCVD is the possibility to use alternative substrate materials such as GaAs or Si rather than the very expensive CdZnTe. We typically use 2-inch, epi-ready, semi-insulating (100) GaAs substrates, oriented 2° off toward the nearest ⟨110⟩. A CdTe film, typically 3–4 μm thick, is deposited prior to the growth of HgCdTe as a buffer layer reducing stress caused by crystal lattice misfit between the GaAs substrate and HgCdTe epitaxial layer structure. The growth is carried out at a temperature of about 350°C and a mercury zone of 210°C. Electronic-grade diisopropyltelluride and dimethylcadmium are used as Te and Cd precursors, respectively. Elemental mercury is used in a quartz bath as an Hg precursor. H_2 is the carrier gas. Tris-dimethylaminoarsenic is used for acceptor doping and it provides *in situ* *p*-type doping in a concentration range between 10^{14} cm^{-3} and 5×10^{17} cm^{-3}. The *n*-type doping is achieved by ethyl iodide with *in situ* control over the doping range from 10^{14} cm^{-3} to 1×10^{18} cm^{-3}. Both elements are well behaved, stable, and slowly diffusing dopants. The growth is completed with a cooling procedure in metal-rich ambient medium. The HgCdTe heterostructures are not annealed, neither during the growth process (*in situ*) nor after the growth (ex situ). More comprehensive details of the growth experiments performed in our laboratory are presented in Refs. 20–23.

Devices presented within the framework of this paper have a p^+-B_p cap-barrier structural unit, intentionally undoped (due to donor background concentration with *n*-type conductivity) or a low *p*-type doped absorption layer and wide band-gap highly doped N^+ bottom contact layer. In a long-wavelength infrared (LWIR) device, cap contact is a combination of highly doped *n*-type and *p*-type

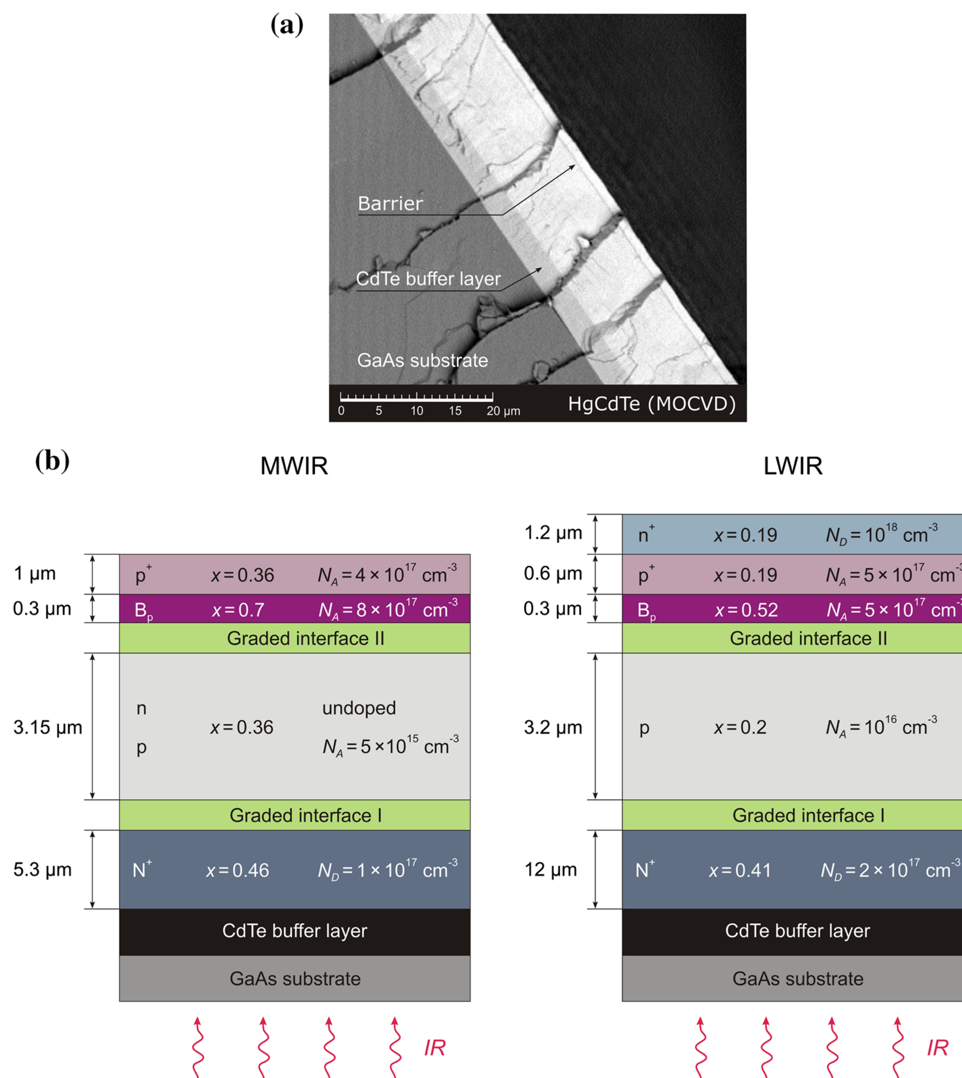

Fig. 2. Typical MOCVD-grown HgCdTe barrier structure: (a) the cleavage profile of the HgCdTe layer and (b) cross-section of the MWIR and LWIR HgCdTe heterostructure with parameters assumed for the growth and modeling. x is the alloy composition, N_A is the acceptor concentration, N_D is the donor concentration.

layers. Such a design should create a tunneling junction to allow for the collection of photogenerated holes. A cap n-type layer provides low-resistance ohmic contact that is especially important in the view of the response time of the device. The schematic cross-section of the $p^+B_pnN^+/p^+B_ppN^+$ mesa device optimized for the mid-wavelength infrared (MWIR) range is illustrated in Fig. 2. The cleavage profile of the HgCdTe layer grown on GaAs substrate and a CdTe buffer layer was taken from an electron microscope. The CdTe buffer and wide bandgap barrier (thin darker layer) can be clearly distinguished in the deposited layer.

Classical heterostructures have been expanded with graded interface layers. Graded doping and composition x layers represent the real structure, whose profile is shaped by interdiffusion processes during $Hg_{1-x}Cd_xTe$ growth at 350°C. Figure 3 shows compositional and dopant profiles for an MWIR HgCdTe $p^+B_ppN^+$ structure, measured using secondary ion mass spectroscopy (SIMS).

After the MOCVD growth, the material was processed into mesa-geometry detectors with circular apertures 300 μm in diameter using standard photolithography and wet chemical etching with 4% bromine solution in glycol to the N^+ bottom contact layer. Au contacts were made to the top of mesa and to the bottom layer. The test devices presented in the paper have not been passivated.

EXPERIMENTAL RESULTS

Barrier detectors presented in this paper were optimized at 50% cut-off wavelengths up to 3.6 μm, 6 μm, and 9 μm at 230 K. The relative spectral response of the devices is presented in Fig. 4. The devices are bottom illuminated (see Fig. 2) through the N^+ layer that plays the role of an infrared

Fig. 4. Relative spectral response for a backside illuminated, thermoelectrically-cooled (230 K) MOCVD-grown HgCdTe barrier detector optimized at 3.6 μm (a), 6 μm (b), and 9 μm (c) cut-off wavelengths. Relative spectral response was calculated on the basis of measured values of current responsivity expressed in (A/W) at bias voltage of −1 V.

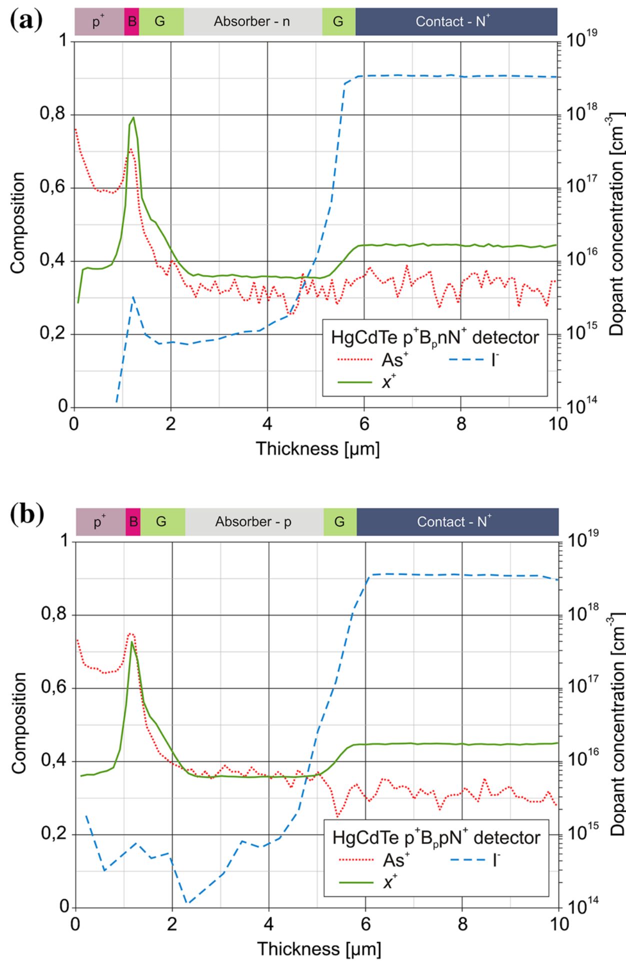

Fig. 3. SIMS measurements of composition and dopant profiles of HgCdTe $p^{+}B_{p}nN^{+}$ (a) and $p^{+}B_{p}pN^{+}$ (b) photodetector grown by MOCVD.

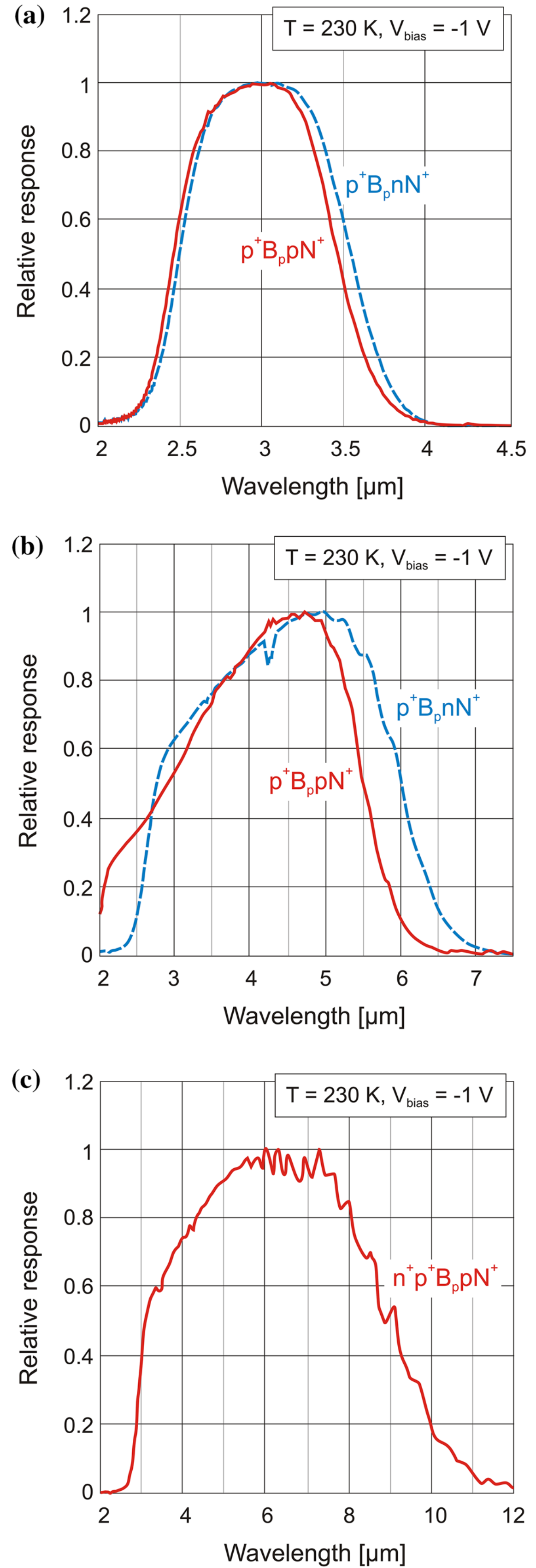

transmitting window for photons with energies below the bandgap. Since diffusion length in the N^{+} layer is short compared to its thickness, the charge carriers generated in the layer do not produce a photocurrent, so the bandgap of the layer determines the cut-on wavelength of the devices.

Figure 5 shows the measured at 230 K and 300 K current–voltage characteristics for MOCVD-grown HgCdTe barrier detectors optimized for different spectral ranges. Reverse biased detectors (both $p^{+}B_{p}nN^{+}$ and $p^{+}B_{p}pN^{+}$) with a 3.6 μm cut-off wavelength exhibited very low dark currents in the range of $(2\text{–}3) \times 10^{-4}$ A/cm^2 at 230 K. The data indicate

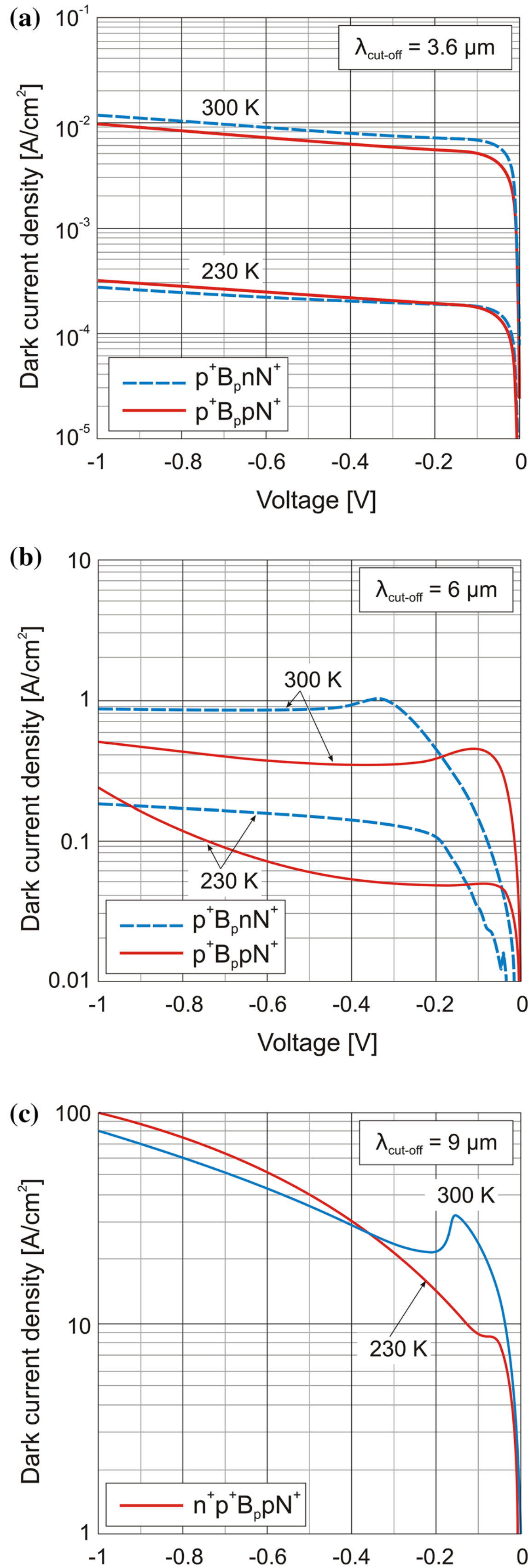

Fig. 5. Current–voltage characteristics for an MOCVD-grown HgCdTe barrier detectors operated at 230 K and 300 K and optimized at 3.6 μm (a), 6 μm (b), and 9 μm (c) cut-off wavelength.

that the dark current is mostly due to diffusion current. This conclusion may be carried out by theoretical data obtained by Reine et al.[24] However, visible gentle rise of dark current with bias is associated with the SRH GR process, which was analyzed in detail by Kopytko et al.[25] Very low threshold voltages (−0.1 V) of this detectors indicate that there is no valence band barrier. $p^+B_ppN^+$ detector with a 6 μm cut-off wavelength and $n^+p^+B_ppN^+$ detector with a 9 μm cut-off wavelength show a suppression of Auger generation that is especially evident at 300 K where the negative dynamic resistance area occurred. Under reverse bias, the electrons are extracted from the absorber region by a positive electrode connected to the bottom N^+-layer. The electrons are also excluded from the absorber near the B_p-p junction because they cannot be injected through the barrier. As a consequence of a electron concentration reduction, the hole concentration also decreases. The exclusion effect is limited by the level of acceptor concentration (electrical carrier neutrality), as well as by thermal generation, which restores the thermal equilibrium state. However, devices with a p-type absorbing layer indicate tunneling, which dominates the leakage current for higher biases. This tunneling effects are especially due to trap assistant tunneling (TAT) at a decisive heterojunction. In $p^+B_ppN^+$ and $n^+p^+B_ppN^+$ detectors, a decisive p–n junction is located at the interface between the lightly doped p-type absorber and the heavily doped N^+ bottom contact layer. TAT currents might occur via SRH GR states in a volume of the devices, and since mesa detectors were not passivated after chemical etching, also on the surface of the devices. A $p^+B_pnN^+$ detector with a 6 μm cut-off wavelength also shows a suppression of Auger generation. However, suppression of Auger mechanisms is much more effective in a p-type absorber than in an n-type. Minority holes are extracted from the n-type absorber at a much slower rate than electrons from a p-type absorber. Thus, a device with an n-type absorbing layer also shows a relatively large threshold voltage.

On the basis of spectral response measurements we determined the peak current responsivity. The peak value of current responsivity was taken at λ_{peak} for each device and plotted as a function of reverse bias voltage on Fig. 6. It is worth pointing out that the maximum response of both detectors optimized at a 3.6 μm cut-off wavelength assumes a constant value of about 2 A/W in the whole range of reverse bias voltage. The large photoresponse at zero bias is due to a diffusion current of

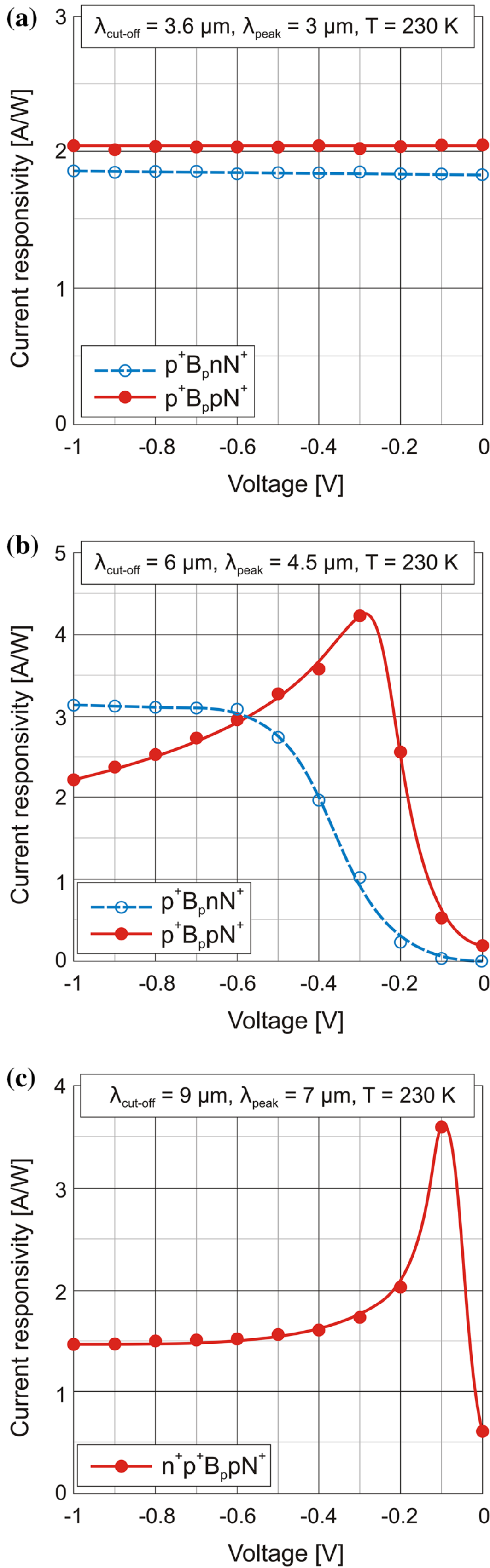

Fig. 6. Peak current responsivity as a function of reverse bias for a backside-illuminated MOCVD-grown HgCdTe barrier detector operated at 230 K and optimized at 3.6 μm (a), 6 μm (b), and 9 μm (c) cut-off wavelengths.

photogenerated carriers in the absorbing layer. This confirms a zero-valence band offset and will result in lower operating bias that is in agreement with the dark current–voltage curves in Fig. 5. The peak value of current responsivity of devices optimized at 6 μm and 9 μm cut-off wavelengths is bias-dependent. Low current responsivity at zero bias is related to a short carrier lifetime. With the increase of reverse bias voltage, carrier lifetime also increases due to suppression of Auger mechanisms. This causes an increase in current responsivity. Exclusion and extraction effects in the *n*-type absorber are much slower, thus an increase in responsivity occurs for higher bias voltages. A further decline in responsivity in devices with a *p*-type absorbing layer is related to a decreasing carrier lifetime due to tunneling mechanisms.

Figure 7 presents the HgCdTe barrier photodiodes time constant as a function of a reverse bias voltage for an operating temperature of 230 K. We can see that unbiased detectors are characterized by relatively long time constant due to the diffusion factor. The time constant of both devices optimized at a 3.6 μm cut-off wavelength decreases with reverse bias. For devices with 6 μm and 9 μm cut-off wavelengths, reverse bias initially increases the response time. The space-charge region extends into the absorber region and the drift transit time becomes dominant. Further increase of the bias voltage reduces the time constant tens of times. The decrease in the time constant becomes faster for biases higher than the threshold voltage. This behavior is directly connected with the depletion in the absorber region. Exclusion and extraction effects cause the ambipolar mobility increases due to a decrease of carrier concentration. What is more, the *p*-type material is characterized by higher ambipolar mobility, and should give fast and efficient drift collection of charge carriers in the absorber area. However, the time constants of reverse-biased MWIR devices, both with *p*- and *n*-type absorbing layers, are comparable and do not fall below 10 ns. Despite that the drift transit across the absorber area can be reduced by applying high reverse bias, the *RC* time constant (arising from the capacitance *C* and the load resistance *R*) increases the response time. This is associated with the finite resistance of the devices arising due to higher contact resistance to the p^+ cap layer. Optimized LWIR architecture with low-resistance ohmic contact to the n^+ cap layer and n^+–p^+ tunneling junction allows for a fast collection of photogenerated carriers. The time constant of the $n^+p^+B_ppN^+$ photodiode

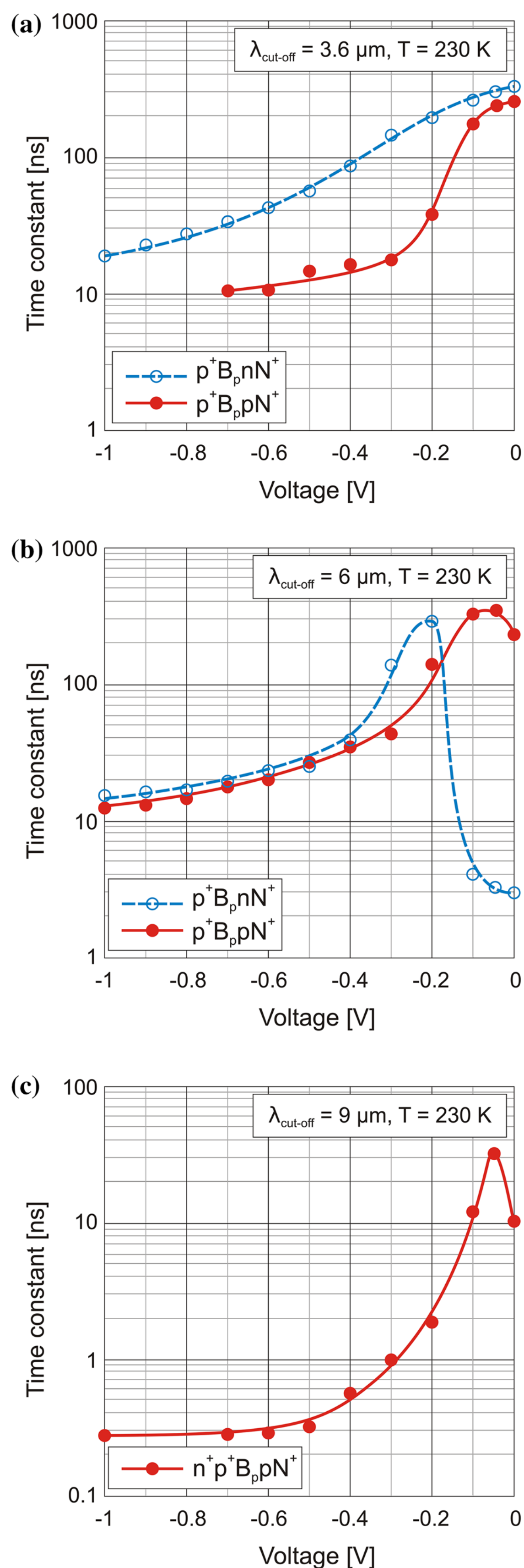

◀Fig. 7. Photodiode signal response time as a function of reverse bias for a backside-illuminated MOCVD-grown HgCdTe barrier detector operated at 230 K and optimized at 3.6 μm (a), 6 μm (b), and 9 μm (c) cut-off wavelengths.

is bias-dependent and falls below 1 ns at −0.3 V. For −0.6 V it reaches a constant value of about 300 ps.

COMPARISON OF THE DETECTOR PERFORMANCE

Figure 8 compares the minimum dark current density of the analyzed structures to the values given by the "Rule 07". "Rule 07" is an empirical relation proposed by Tennant et al.[26] for the best molecular beam epitaxy-grown HgCdTe double-layer planar heterostructure technology with *p*-on-*n* configuration. It describes the dark-current behavior for a wide range of temperatures and wavelengths. Other barrier-type devices fabricated on the basis of III–V materials[4,16,27–30] were also compared to the "Rule 07".

Dark current density values were chosen for specific operating points at threshold voltages. For devices indicating negative dynamic resistance, operating points were chosen for voltages where dark currents assume their minimum values. Our detectors optimized at a 3.6 μm cut-off wavelength show an order of magnitude lower dark current densities than those determined by "Rule 07". Specific barrier architecture with a combination of Auger-suppression is characterized by a low thermal generation. Such promising results for devices with a cut-off wavelength up to 3.6 μm prompted us to devise a similar design for the larger cut-off wavelengths up to 6 μm and then 9 μm. Dark current densities of this devices are close to the values given by "Rule 07".

Figure 9 compares the detectivity (D^*) of non-immersed HgCdTe barrier detectors (red dashed lines) with the optically immersed HgCdTe photodiodes manufactured by Vigo System S.A. (dark-solid lines). The highest achieved values so far at 230 K are pointed by single white points. The detectivity of HgCdTe detectors with *p*-type barriers is comparable to the value-marked HgCdTe photodiodes. However, well-designed optically immersed devices approach the background-limited infrared photodetection (BLIP) performance while thermoelectrically cooled with 2-stage Peltier coolers. In this case the detectivity is proportional to n^2, where n is the refractive index equal to 3.4 for GaAs substrates/lenses. Thus, implementing the optical immersion for HgCdTe barrier detectors might increase the detectivities by an order of magnitude.

In our experiment, the detectivity was determined for the operating points at which the

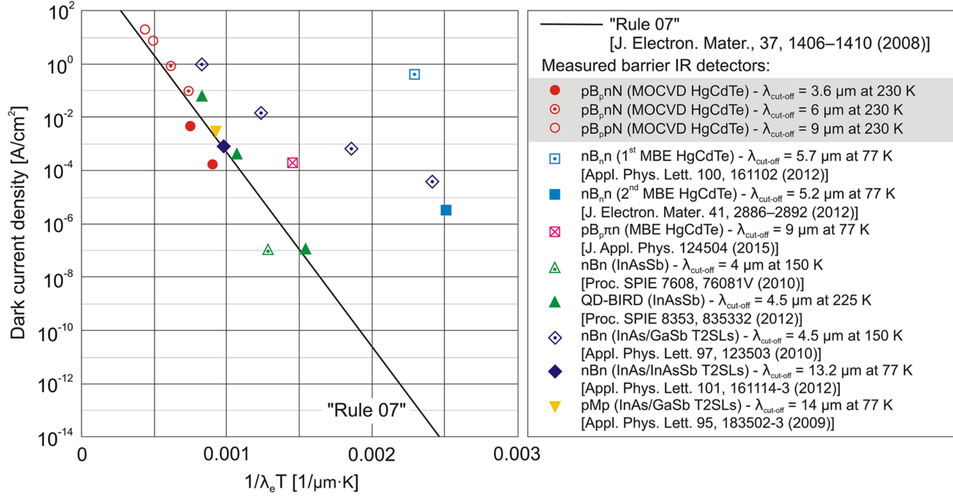

Fig. 8. Comparison of different barrier IR detectors to the "Rule 07". Devices fabricated in our laboratory are marked with a darker field on the legend.

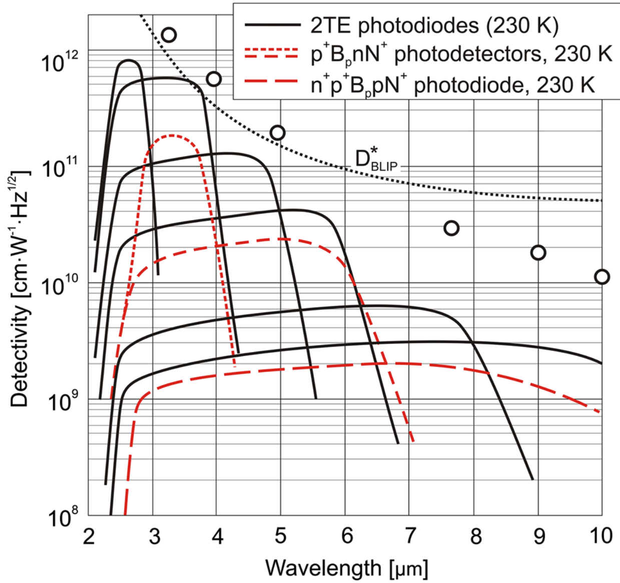

Fig. 9. Comparison of spectral detectivity of HgCdTe barrier detectors (red dashed lines) with HgCdTe optically immersed photodiodes (dark-solid lines) with 2-stage TE coolers manufactured by Vigo System S.A. The best HgCdTe experimental data (white dots) are measured for detectors with a FOV equal to 36°. BLIP detectivity is calculated for FOV = 2π.

analyzed detectors reach the maximum current responsivity and minimum dark current values, on the basis of the expression:

$$D^* = \frac{R_i}{i_n(V)}\sqrt{A} \quad (1)$$

where R_i is the current responsivity and $i_n(V)$ is the noise current. The calculated noise current was assumed to be dependent on thermal Johnson–Nyquist noise and electrical shot noise due to dark current:

$$i_n(V) = \sqrt{4k_\mathrm{B}T/R + 2qI_\mathrm{D}} \quad (2)$$

where R is the dynamic resistance, I_D is the dark current, T is the temperature, and k_B is the Boltzmann constant.

THEORETICAL MODELING

Detailed numerical simulations were applied to explain the dark current plots of the experimental data of the LWIR n^+p$^+$B$_p$$pN^+$ photodiode. Theoretical modeling of the HgCdTe heterostructures requires the solution of a set of transport equations that are comprised of the Poisson's and the electron/hole current continuity equations. In our simulation procedure we have used a commercially available software APSYS platform (Crosslight Inc.). The applied model incorporates a wide spectrum of GR processes determined by the HgCdTe electrical properties including Auger 1, Auger 7, SRH, as well as BTB and TAT tunneling mechanisms. In TAT simulation the Hurkx et al. model was implemented.[31] The detailed description of specific equations used in drift–diffusion (D–D) model can be found in APSYS manual.[32] All HgCdTe parameters used in calculation of recombination rates are described in detail in Capper's monograph.[33] Table I presents chosen structural parameters taken in numerical modeling of the LWIR HgCdTe $n^+p^+B_ppN^+$ heterostructure.

HgCdTe is a narrow-gap semiconductor exhibiting a non-parabolic conduction band and high carrier degeneracy. To overcome numerical problems with computation of the Fermi–Dirac integral for a non-parabolic model, Quan et al. and Wang et al. have proposed approximations to this expression.[34,35] However, this model is fulfilled for temperatures from 77 K to 120 K, and thus has not been fully validated for HOT conditions. At

Table I. Parameters taken in modeling of the LWIR HgCdTe $n^{+}p^{+}B_{p}pN^{+}$ heterostructure

	N^+	P^+	B_p	G	P	G	N^+
Concentration, N_D, N_A (cm^{-3})	10^{18}	5×10^{17}	5×10^{17}	$5 \times 10^{17} \rightarrow 10^{16}$	10^{16}	$10^{16} \rightarrow 2 \times 10^{17}$	2×10^{17}
Doping concentration's gauss tail, dx (μm)				0.02			
Composition, x	0.19	0.19	0.52	$0.2 \rightarrow 0.52$	0.2	$0.2 \rightarrow 0.41$	0.41
Geometry, d (μm)	1	0.6	0.2	1	3.2	0.5	10
Trap concentration, N_T (cm^{-3})				10^{14}			
Trap ionisation energy, E_T				$1/3E_g$			
Capture coefficient, c_n, c_p (cm^3 s^{-1})				1.5×10^{-7}, 3×10^{-9}			
Device electrical area, A (μm^2)				100×100			
Overlap matrix F_1F_2				0.3			
Incident power, P (W m^{-2})				500			

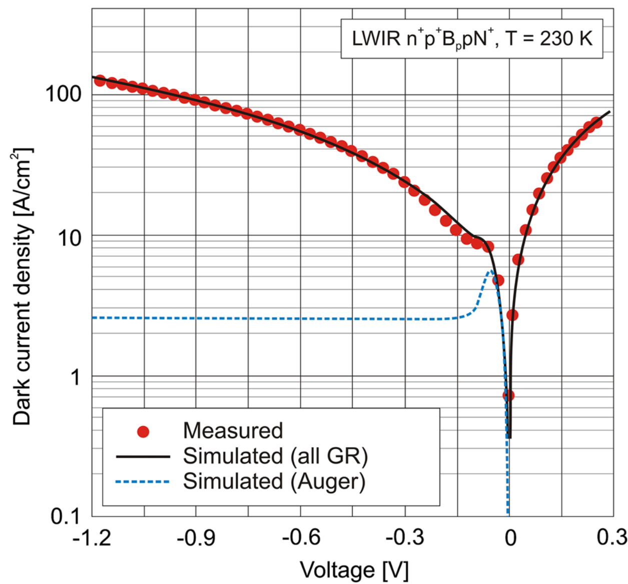

Fig. 10. Simulated dark current density for graded gap HgCdTe $n^{+}p^{+}B_{p}pN^{+}$ photodiode. Simulations were performed for Auger, SRH, BTB, and TAT mechanisms at decisive heterojunctions.

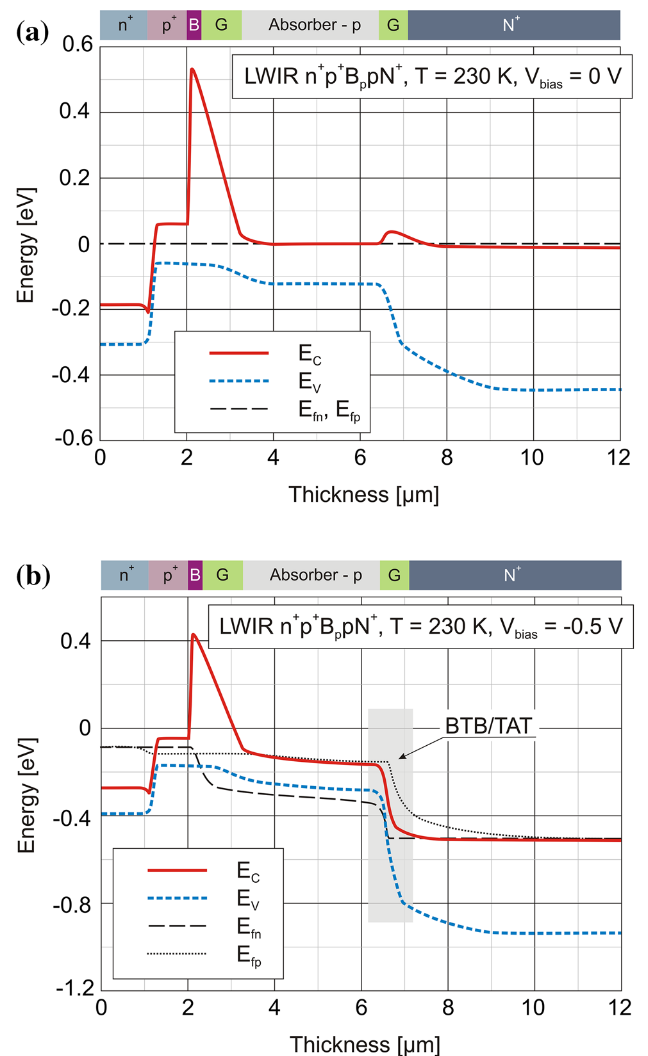

Fig. 11. Simulated band diagram of a graded gap HgCdTe $n^{+}p^{+}B_{p}pN^{+}$ photodiode for (a) zero and (b) 500 mV reverse-bias conditions.

increased temperatures of about 230 K, the Fermi–Dirac statistics for a non-degenerate semiconductor model with parabolic energy bands gives quite good results in a broad range of doping concentrations.[36]

Calculated dark current characteristics are presented in Fig. 10. Simulations were performed including all GR mechanisms (solid line): Auger, SRH, as well as BTB and TAT tunneling mechanisms to fit the experimental results. As we can see, in a wide region of bias voltages, an excellent agreement between experimental and calculated results has been obtained. What is more, the Auger part of the dark current was also plotted (dashed line). In the case of good quality p-type materials with very low structural defects, the influence of Auger processes might be reduced by exclusion and extraction effects. For large voltages, the presented dark current density versus voltage indicates the tunneling effects. BTB and/or field-enhanced TAT via traps located at dislocation cores as well as mercury vacancies at the decisive heterojunctions

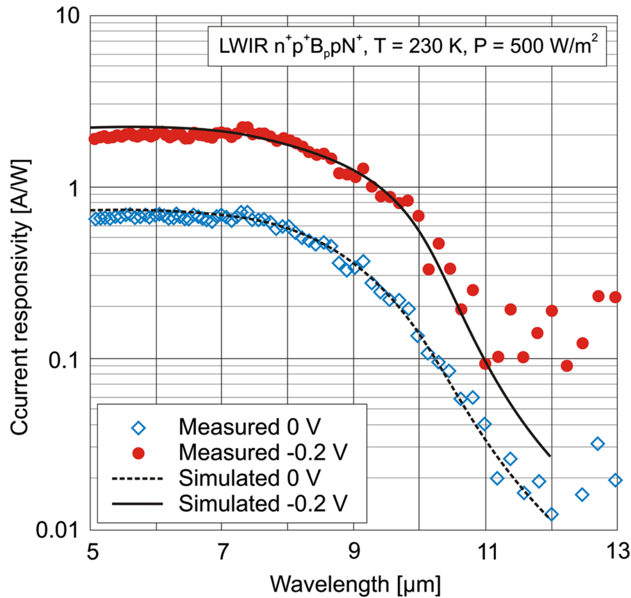

Fig. 12. Simulated current responsivity for a graded gap HgCdTe $n^+p^+B_ppN^+$ photodiode. Simulations were performed for Auger, SRH, BTB, and TAT mechanisms at decisive heterojunctions.

seems to be the most important mechanism of dark current generation at larger reverse biases.

Figure 11 presents calculated bandgap diagrams of the simulated $n^+p^+B_ppN^+$ photodiode for zero and −0.5 V bias. Bandgap diagrams under reverse bias clearly shows that the tunneling mechanism at the absorber and bottom contact heterojunction determine the device performance, especially currents above −0.1 V. The measured and simulated spectral response characteristics are presented in Fig. 12. The maximum responsivity is estimated for a λ_{peak} = 7 μm. The device was assumed to be back-side-illuminated with an incident power of 500 W/m^2. The absorption of IR radiation occurs in the *p*-type absorber and wider-gap bottom contact layer.

CONCLUSIONS

As it was shown in this paper, it is possible to provide zero-valence band offset in HgCdTe barrier detectors manufactured using MOCVD technology. Thanks to the barriers, dark current could be effectively reduced in the presented structures (p^+–B_p cap-barrier structural unit), with maintained high responsivity.

The $p^+B_pnN^+$ structure optimized at a 3.6 μm cut-off wavelength at 230 K shows an order of magnitude lower dark currents than those determined by "Rule 07". The device exhibited dark current densities at the range of (2–3) × 10^{-4} A/cm^2 at 230 K and the maximum current responsivity of about 2 A/W. The device shows a zero-valence band offset. Due to the large photoresponse at zero bias and very low threshold voltage, operation at near-zero bias is possible.

Promising results for devices with a cut-off wavelength up to 3.6 μm prompted us to devise a similar design for the slightly larger cut-off wavelength up to 6 μm and then 9 μm. This device shows a suppression of Auger generation that is especially evident at 300 K, which causes dark current densities to be close to the values given by "Rule 07". The suppression of Auger mechanisms is highly effective in devices with a *p*-type absorber. However, these devices indicate tunneling, which dominates leakage current for higher biases. These tunneling effects are particularly due to TAT at a decisive heterojunction. Tunneling effects also lead to a reduction of current responsivity.

Despite serious competition from alternative technologies, HgCdTe is unlikely to be seriously challenged in the next decade for high-performance applications. Further work requires improvement in the time constant of MWIR HgCdTe barrier detectors, as well as limiting the tunneling effect in LWIR devices.

ACKNOWLEDGEMENTS

The work has been carried out under the financial support of the Polish National Science Centre as research Projects No. DEC-2013/08/M/ST7/00913 and DEC-2013/08/A/ST5/00773.

OPEN ACCESS

This article is distributed under the terms of the Creative Commons Attribution 4.0 International License (http://creativecommons.org/licenses/by/4.0/), which permits unrestricted use, distribution, and reproduction in any medium, provided you give appropriate credit to the original author(s) and the source, provide a link to the Creative Commons license, and indicate if changes were made.

REFERENCES

1. White, "Infrared detectors," U.S. Patent 4,679,063 (22 September 1983).
2. S. Maimon and G.W. Wicks, *Appl. Phys. Lett.* 89, 151109 (2006).
3. P. Klipstein, *Proc. SPIE* 6940, 69402U (2008).
4. P. Klipstein, O. Klin, S. Grossman, N. Snapi, B. Yaakobovitz, M. Brumer, I. Lukomsky, D. Aronov, M. Yassen, B. Yofis, A. Glozman, T. Fishman, E. Berkowicz, O. Magen, I. Shtrichman, and E. Weiss, *Proc. SPIE* 7608, 76081V (2010).
5. P. Martyniuk, M. Kopytko, and A. Rogalski, *Opto-Electron. Rev.* 22, 127 (2014).
6. A.M. Itsuno, J.D. Phillips, and S. Velicu, *Appl. Phys. Lett.* 100, 161102 (2012).
7. A.M. Itsuno, J.D. Phillips, and S. Velicu, *J. Electron. Mater.* 41, 2886 (2012).
8. S. Velicu, J. Zhao, M. Morley, and A.M. Itsuno, J.D. Philips, *Proc. SPIE* 8268, 82682X-1 (2012).
9. M. Kopytko, J. Wróbel, K. Jóźwikowski, A. Rogalski, J. Antoszewski, N.D. Akhavan, G.A. Umana-Membreno, L. Faraone, and C.R. Becker, *J. Electron. Mater.* 44, 158 (2014).
10. N.D. Akhavan, G. Jolley, G.A. Umma-Membreno, J. Antoszewski, and L. Faraone, *IEEE Trans. Electron Devices* 61, 3691 (2014).

11. N.D. Akhavan, G. Jolley, G.A. Umma-Membreno, J. Antoszewski, and L. Faraone, *IEEE Trans. Electron Devices* 62, 722 (2015).
12. A. Rose, *Concepts in Photoconductivity and Allied Problems* (New York: Interscience Publishers, 1963).
13. M. Kopytko, A. Kębłowski, W. Gawron, P. Madejczyk, A. Kowalewski, and K. Jóźwikowski, *Opto-Electron. Rev.* 21, 402 (2013).
14. N.D. Akhavan, G.A. Umana-Membreno, G. Jolley, J. Antoszewski, and L. Faraone, *Appl. Phys. Lett.* 105, 121110 (2014).
15. O. Gravrand, F. Boulard, A. Ferron, Ph. Ballet, and W. Hassis, *J. Electronic Materials* 44, 3069 (2015).
16. W.C. Qiu, T. Jiang, and X.A. Cheng, *J. Appl. Phys.* 118, 124504 (2015).
17. M. Kopytko, A. Kębłowski, W. Gawron, A. Kowelewski, and A. Rogalski, *IEEE Trans. Electron Devices* 61, 3803 (2014).
18. M. Kopytko, A. Kębłowski, W. Gawron, P. Martyniuk, P. Madejczyk, K. Jóźwikowski, A. Kowalewski, O. Markowska, and A. Rogalski, *Opt. Eng.* 54(10), 105105-7 (2015).
19. M. Kopytko, A. Kębłowski, W. Gawron, and W. Pusz, *Semicond. Sci. Technol.* 31, 035025 (2016).
20. P. Madejczyk, A. Piotrowski, W. Gawron, K. Kłos, J. Pawluczyk, J. Rutkowski, J. Piotrowski, and A. Rogalski, *Opto-Electron. Rev.* 13, 239 (2005).
21. A. Piotrowski, P. Madejczyk, W. Gawron, K. Kłos, J. Pawluczyk, J. Rutkowski, J. Piotrowski, and A. Rogalski, *Infrared Phys. Technol.* 49, 173 (2007).
22. P. Madejczyk, A. Piotrowski, K. Kłos, W. Gawron, J. Rutkowski, and A. Rogalski, *Opto-Electron. Rev.* 18, 271 (2010).
23. A. Piotrowski and K. Kłos, *J. Electron Mater.* 36, 1052 (2007).
24. M. Reine, J. Schuster, B. Pinkie, and E. Bellotti, *J. Electron Mater.* 42, 3015 (2013).
25. M. Kopytko and K. Jóźwikowski, *IEEE Trans. Electron Devices* 61, 3803 (2015).
26. W.E. Tennant, D. Lee, M. Zandian, E. PiQuette, and M. Carmody, *J. Electron. Mater.* 37, 1406 (2008).
27. D.Z. Ting, A. Soibel, C.J. Hill, S.A. Keo, J.M. Mumolo, and S.D. Gunapala, *Proc. SPIE* 8353, 835332 (2012).
28. E. Plis, S. Myers, M.N. Kutty, J. Mailfert, E.P. Smith, S. Johnson, and S. Krishna, *Appl. Phys. Lett.* 97, 123503 (2010).
29. H.S. Kim, O.O. Cellek, Z.-Y. Lin, Z.-Y. He, X.-H. Zhao, S. Liu, H. Li, and Y.H. Zhang, *Appl. Phys. Lett.* 101, 161114-3 (2012).
30. B.M. Nguyen, S. Bogdanov, S. Abdollahi Pour, and M. Razeghi, *Appl. Phys. Lett.* 95, 183502 (2009).
31. G.A. Hurkx, D.B.M. Klaassen, and M.P.G. Knuvers, *IEEE Trans. Electron Devices* 39, 2 (1992).
32. *APSYS Macro/User's Manual*, Ver. 2011 (Crosslight Software Inc., 2011).
33. P.P. Capper, *Properties of Narrow Gap Cadmium-based Compounds* (London: Inst. Elect. Eng, 1994).
34. Z.J. Quan, G.B. Chen, L.Z. Sun, Z.H. Ye, Z.F. Li, and W. Lu, *Infrared Phys. Technol.* 50, 1 (2007).
35. J. Wang, X. Chen, W. Hu, L. Wang, Y. Chen, W. Lu, and F. Xu, *Proc. SPIE* 8012, 80123B (2011).
36. J. Wenus, J. Rutkowski, and A. Rogalski, *IEEE Trans. Electron Devices* 48, 7 (2001).